

Rare Self-Luminous Mixed-Valence Eu-MOF with a Self-Enhanced Characteristic as a Near-Infrared Fluorescent ECL Probe for Nondestructive Immunodetection

Lu Zhao, Xianzhen Song, Xiang Ren, Dawei Fan, Qin Wei, and Dan Wu*

Cite This: *Anal. Chem.* 2021, 93, 8613–8621

Read Online

ACCESS |



Metrics & More

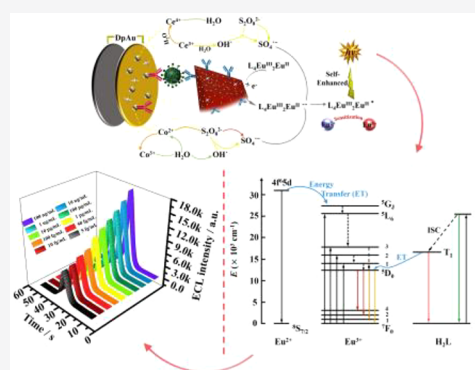


Article Recommendations



Supporting Information

ABSTRACT: Steady and efficient sensitized emission of Eu^{2+} to Eu^{3+} can be achieved through a rare mixed-valence Eu-MOF ($\text{L}_4\text{Eu}^{\text{III}}_2\text{Eu}^{\text{II}}$). Compared with the sensitization of other substances, the similar ion radius and configuration of the extranuclear electron between Eu^{2+} and Eu^{3+} make sensitization easier and more efficient. The sensitization of Eu^{2+} to Eu^{3+} is of great assistance for the self-enhanced luminescence of $\text{L}_4\text{Eu}^{\text{III}}_2\text{Eu}^{\text{II}}$, the longer luminous time, and the more stable electrochemiluminescence (ECL) signal. Simultaneously, $\text{L}_4\text{Eu}^{\text{III}}_2\text{Eu}^{\text{II}}$ possesses near-infrared (NIR) fluorescence of around 900 nm and a mighty self-luminous characteristic, which render it useful as a NIR fluorescent probe and as a luminophore to establish a NIR ECL biosensor. This NIR biosensor can greatly reduce the damage to the detected samples and even achieve a nondestructive test and improve the detection sensitivity by virtue of strong susceptibility and environmental suitability of NIR. In addition, the $\text{CeO}_2@\text{Co}_3\text{O}_4$ triple-shelled microspheres further enhanced the ECL intensity due to two redox pairs of $\text{Ce}^{3+}/\text{Ce}^{4+}$ and $\text{Co}^{2+}/\text{Co}^{3+}$. The NIR ECL biosensor based on these strategies owns an ultrasensitive detection ability of CYFRA 21-1 with a low limit of detection of 1.70 fg/mL and also provides a novel idea for the construction of a highly effective nondestructive immunodetection biosensor.



INTRODUCTION

Near-infrared fluorescent probes (NIFPs) exhibit unique optical and operational properties that make them an excellent selection for immunoassay,¹ environmental pollutant analysis,² and medical imaging.³ Probes can improve tissue penetration and reduce damage to the matrix.⁴ Furthermore, the NIFPs, whose region of spectrum is 800–1700 nm, can avoid the interference of visible fluorescence and heighten the accuracy of the immunoassay^{4,5} and can afford nondestructive analysis as well as availability under harsh conditions.⁶ By means of electrochemistry and related instruments, the sensitivity of detection and analysis that participated by NIFPs has advanced rapidly, and the information presented is also more intuitive. By virtue of its broad dynamic ranges, outstanding sensitivity and stability, convenient operation, benign time, and space control over the light emission,^{6,7} electrochemiluminescence (ECL) has managed to outsmart other ways that can be combined with NIFPs and has become one of the most suitable for detection.⁸ Nevertheless, the eminent bottleneck remains in the same luminescent intensity of NIFPs, which played the role of ECL luminophores. Therefore, exploiting a NIFP that possessed a doughty luminous efficiency as the ECL luminophore for highly efficient immunoassay is an area deserving research.

Compared to other NIFP materials, the optical properties of near-infrared (NIR) lanthanide complexes, unlike that of organic fluorophores and semiconductor nanoparticles, possess amazing complementary superiorities, which have become a research hotspot.⁹ In terms of Ln-MOFs powered by tunable luminescence properties, long luminescent lifetimes, and forceful energy transfer ability, the assistance of a sensitizer is highly effective for realizing the enhancement luminescence of Ln^{3+} and spectrum control.^{10–13} The reported sensitizers include Ln^{3+} ,¹⁰ semiconductors,^{11,12} organic matters,¹³ and so on. Among them, sensitization between Ln^{3+} is the most common. The enhanced luminescence effect stems from the energy transfer of the sensitizer and luminescent Ln^{3+} .^{10–13} One situation is that the 4f electronic layer of optically inert lanthanide metal counterions such as La^{3+} ,¹⁴ Gd^{3+} ,¹⁵ and Y^{3+} ¹⁶ is in a stable state of full or half-empty, and their low probability of trapping electron results in that the ligand cannot effectively transfer energy to them but only to luminous

Received: April 11, 2021

Accepted: June 3, 2021

Published: June 11, 2021



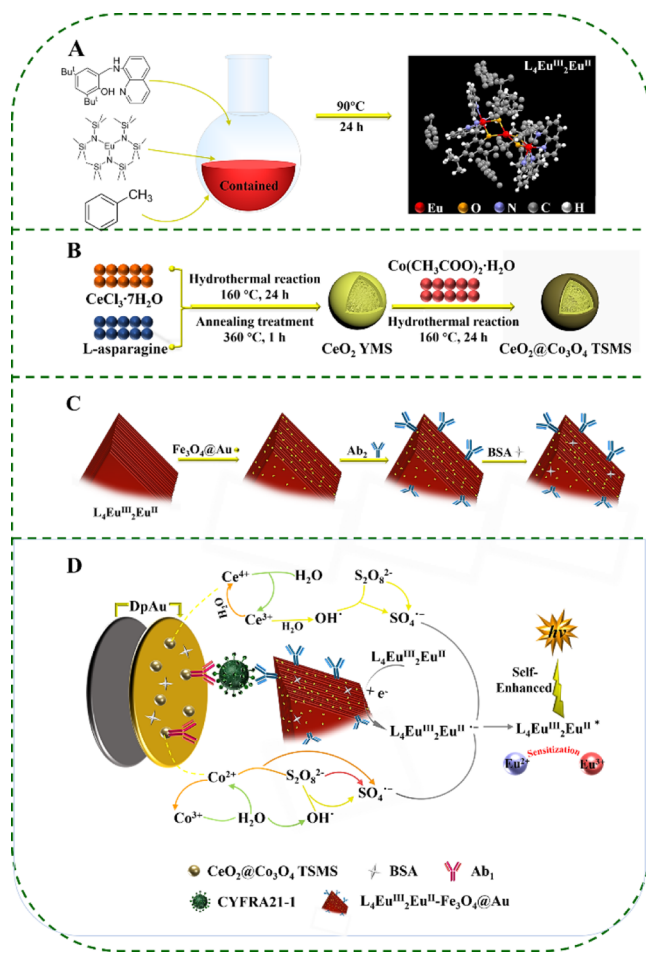
ions such as Eu^{3+} and Tb^{3+} , thus enhancing the characteristic fluorescence of Eu^{3+} and Tb^{3+} . Otherwise, luminescent Ln^{3+} ions can also implement sensitization by embedding in a subjectual host in the form of doping,^{11,12} in which the sensitized ion and doped sensitizer have similar ion radius and configuration of extra-nuclear electron, which may further strengthen the effect of the doped ions in synergistic energy transfer, such as the sensitization of Tb^{3+} to Eu^{3+17} and Ce^{3+} to Tb^{3+} .¹⁸ Based on this preponderance, we speculated that it is easier to achieve sensitization between Eu^{2+} and Eu^{3+} . Fortunately, we found a rare mixed-valence Eu-MOF to solve the eminent bottleneck in the instability of Eu^{2+} on account of its strong reducibility oxidized to Eu^{3+} . The inclusive sensitization of Eu^{2+} to Eu^{3+} can achieve self-enhanced luminescence to enhance ECL efficiency.

There is little doubt that coreaction accelerators that catalyzed the further generation of coreactant radicals are likewise the vital link of the whole ECL process. The efficiency of charge utilization is conclusive for the whole performance of catalysis. A good catalytic activity can be realized effectually via an ideal platform offered by the core-shell structure, which has sufficient diffusion channels and a large active specific surface area to possess high conductivity and resistance to reunite.^{19,20}

Among these core-shell structure materials, the CeO_2 microsphere has gained massive attention with merits of its ultrahigh electrocatalytic activity resulted from the inherent $\text{Ce}^{3+}/\text{Ce}^{4+}$ redox pair and remarkable durability in water.^{21,22} Surprisingly, the catalytic performance will be further promoted through the synergistic effect between CeO_2 and metal oxides (e.g., TiO_2 ,²³ Co_3O_4 ,²¹ Fe_2O_3 ,²⁴ and NiO).²⁵ The change in the valence of $\text{Ce}^{3+}/\text{Ce}^{4+}$ and $\text{Co}^{2+}/\text{Co}^{3+}$ can promote more production of coreactant radicals; therefore, the combination of Co_3O_4 and CeO_2 has high-efficiency catalytic capacity to improve the ECL intensity.^{21,22}

All in all, a sandwich-type NIR ECL biosensor, made up of a mixed-valence trinucleate MOF ($\text{L}_4\text{Eu}^{\text{III}}_2\text{Eu}^{\text{II}}$) as NIFP as well as a luminophore and a triple-shelled microsphere (TSMS) ($\text{CeO}_2@\text{Co}_3\text{O}_4$) as the coreaction accelerator, was first formed to achieve an ultrasensitive detection of CYFRA 21-1. CYFRA 21-1 is a tumor marker, which is a full-length fragment of cytokeratins 19 distributed on the surface of normal tissues, such as lamellar or squamous epithelium. It possesses a major significance to productively monitor lung adenocarcinoma and lung squamous cell carcinoma and also breast, bladder, and ovarian cancer.^{26,27} Among the as-fabricated biosensors, $\text{L}_4\text{Eu}^{\text{III}}_2\text{Eu}^{\text{II}}$ as a signal probe was synthesized with a quinolinyl aminophenol ligand 3,5-Bu₂-2-(OH)C₆H₂CH₂NH-8-C₉H₆N (H_2L) and $\text{Eu}[\text{N}(\text{SiMe}_3)_2]_3(\mu\text{-Cl})\text{Li}(\text{THF})_3$ relied on the amine elimination reaction,²⁸ and the synthesis mechanism is shown in Scheme 1. The antenna effect that emerged from the two coordination environments ligand H_2L with a strong conjugate effect conveyed energy to $\text{Eu}^{2+/3+}$, and subsequently, Eu^{2+} sensitized Eu^{3+} , thus stimulating Eu^{3+} to provide strength and steady luminescence. Strong synergistic effects and interface effects between $\text{Ce}^{3+}/\text{Ce}^{4+}$ and $\text{Co}^{2+}/\text{Co}^{3+}$ make $\text{CeO}_2@\text{Co}_3\text{O}_4$ TSMSs own a robust oxygen storage/release capacity, so more $\text{S}_2\text{O}_8^{2-}$ was catalyzed to generate more $\text{SO}_4^{\bullet-}$ radicals, which then react with more $\text{L}_4\text{Eu}^{\text{III}}_2\text{Eu}^{\text{II}}$ to enhancing ECL. This double enhancement approach, which was carried out using $\text{L}_4\text{Eu}^{\text{III}}_2\text{Eu}^{\text{II}}$ and $\text{CeO}_2@\text{Co}_3\text{O}_4$ TSMSs, contributed excellent ECL performance to the as-fabricated biosensor. The broad detection range was from 5 fg/mL to 100 ng/mL and a low limit of detection (LOD) was 1.70 fg/mL.

Scheme 1. Synthesis Routes of (A) $\text{L}_4\text{Eu}^{\text{III}}_2\text{Eu}^{\text{II}}$, (B) $\text{CeO}_2@\text{Co}_3\text{O}_4$ TSMS, (C) $\text{L}_4\text{Eu}^{\text{III}}_2\text{Eu}^{\text{II}}-\text{Fe}_3\text{O}_4@\text{Au}-\text{Ab}_2$ Probe, and (D) the ECL Biosensor Fabrication and Conjectural Mechanism Illustration in $\text{K}_2\text{S}_2\text{O}_8$



EXPERIMENTAL SECTION

Preparation of $\text{Eu}[\text{N}(\text{SiMe}_3)_2]_3$. 12.6778 g of $\text{EuCl}_3 \cdot 6\text{H}_2\text{O}$ was added into 100 mL of lithium bis(trimethylsilyl)amide (24% soln in tetrahydrofuran). With continuous stirring for 24 h at 0 °C, the resulting muddy product was dried under vacuum (0.8 MPa) for 3 days to obtain a yellowish solid. The yellowish solid was recrystallized three times in *n*-pentane to obtain white needle-like crystals, which were dried overnight at 60 °C to obtain the product $\text{Eu}[\text{N}(\text{SiMe}_3)_2]_3$.

Preparation of Quinolinyl Aminophenol. 3.07 g of 8-aminoquinoline was added into 50 mL of methanol, and then, two drops of formic acid was added in this mixed solution and stirred thoroughly until the black solids were dissolved, which was named solution a. 5.0 g of 3,5-di-*tert*-butyl-2-hydroxybenzaldehyde was added into 100 mL of methanol, and the mixed solution b formed after sufficient stirring. Next, solution a was mixed into the stirring solution b and then heated to reflux at 70 °C for 12 h. Finally, the orange solid was harvested by centrifugation and washed with methanol and dried at 60 °C.

Preparation of $\text{L}_4\text{Eu}^{\text{III}}_2\text{Eu}^{\text{II}}$. 0.73 g of the prepared H_2L was dissolved in 5 mL of toluene, which was named solution a. 1.27 g of the prepared $\text{Eu}[\text{N}(\text{SiMe}_3)_2]_3$ was dissolved in 5 mL of toluene, which was named solution b. Solution a is slowly added to the stirring solution b, and then, the mixed solution is

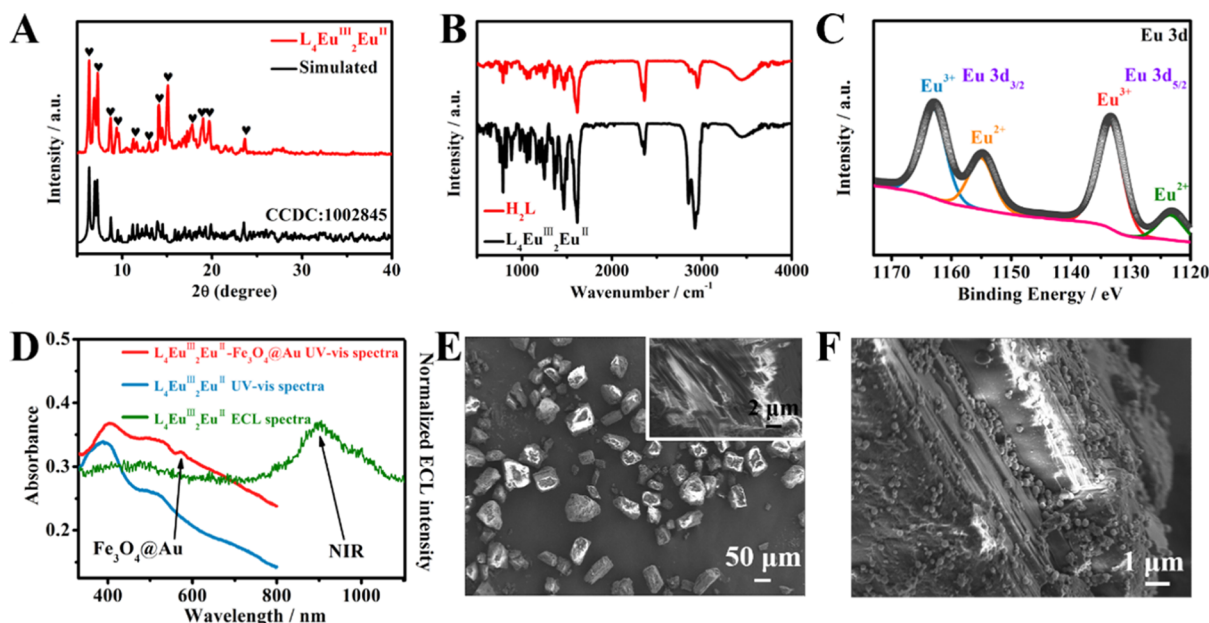


Figure 1. (A) XRD pattern of the as-synthesized and simulated $L_4Eu^{III}_2Eu^{II}$. (B) FT-IR spectra of the H_2L ligand and $L_4Eu^{III}_2Eu^{II}$. (C) XPS spectra in the Eu 3d regions for $L_4Eu^{III}_2Eu^{II}$. (D) UV-vis spectra of $L_4Eu^{III}_2Eu^{II}$ (blue) and $L_4Eu^{III}_2Eu^{II}-Fe_3O_4@Au$ (red) and ECL spectra of $L_4Eu^{III}_2Eu^{II}$ (green). (E) Low- and high-magnification SEM images of $L_4Eu^{III}_2Eu^{II}$. (F) SEM image of $L_4Eu^{III}_2Eu^{II}-Fe_3O_4@Au$.

stirred at 90 °C for 24 h to obtain a deep red solution. The dark red solution was centrifuged to remove the precipitate, and then, the supernatant was placed at 0 °C for 14 days to obtain dark red crystals of $L_4Eu^{III}_2Eu^{II}$.

Preparation of CeO_2 Yolk Microspheres. 6.7 mmol L -asparagine was dissolved in 40 mL of distilled water, and then, 6.7 mmol $CeCl_3 \cdot 7H_2O$ was mixed and stirred vigorously for 15 min, and the solution was transferred into a Teflon-lined stainless steel autoclave and heated at 160 °C in an oven for 24 h. The white solid was harvested by centrifugation and washed with water and ethanol and dried at 60 °C. Finally, the white solid was calcined at 360 °C for 1 h in an air atmosphere to obtain a bright yellow CeO_2 precursor.

Preparation of $CeO_2@Co_3O_4$ TSMs. 0.0931 g of $Co(CH_3COO)_2 \cdot H_2O$ was dissolved in 32 mL of ethanol and stirred to obtain a pink transparent solution. 0.1 g of CeO_2 precursor was added to the above solution, stirred, and ultrasonicated for 8 min to obtain a suspension which was transferred into a Teflon-lined stainless steel autoclave and heated at 120 °C in an oven for 12 h. After the solution was cooled, it was washed three times with deionized water and dried at 80 °C for 12 h to obtain gray-brown $CeO_2@Co_3O_4$ TSMs.

Fabrication Process of the Biosensor. The fabrication of the sensing interface is shown in Scheme 1. The bare glassy carbon electrode (GCE) was brightened with polishing powders such that it achieved a smooth mirror surface level at the beginning. Second, a thin film of Au was electro-deposited on the electrode surface by using $H AuCl_4$ (1%) solution. Then, 10 μL of the as-prepared $CeO_2@Co_3O_4$ solution was coated on the substrate successively. After dyeing, the 8 μL Ab_1 solution (100 $\mu g/mL$) was modified onto the $Au-CeO_2@Co_3O_4$ superstratum and incubation was carried out at 4 °C for 1.5 h. Then, 5 mL of bovine serum albumin (BSA) was dropped on the above-modified electrodes to expose the active site. In the following step, electrodes were covered with 5 μL of diverse concentrations of CYFRA 21-1

and then 5 μL of $L_4Eu^{III}_2Eu^{II}-Fe_3O_4@Au-Ab_2$, respectively, and the modified electrodes were incubated under the same conditions. Finally, the biosensor was successfully constructed.

ECL Detection of CYFRA 21-1. The ECL behavior was monitored over the scanning range of $-1.8-0$ V in 15 mL of phosphate-buffered saline (PBS) (pH = 7.4) containing 80 mM $K_2S_2O_8$ at a photomultiplier tube voltage of 800 V and at a scanning rate of 100 mV/s. The concentrations of $L_4Eu^{III}_2Eu^{II}$ solution and $CeO_2@Co_3O_4$ were 6 and 8 mg/mL, respectively.

RESULTS AND DISCUSSION

Characterizations of $L_4Eu^{III}_2Eu^{II}-Fe_3O_4@Au$ Probes.

First, powder X-ray diffraction (XRD) patterns showed the successful synthesis of $L_4Eu^{III}_2Eu^{II}$. From Figure 1A, we can see that well crystallinity exists in the as-synthesized $L_4Eu^{III}_2Eu^{II}$ and forceful peaks matched with the simulated spectrogram (CCDC-1002845) faultlessly, which were shown at 6.34, 6.96, 7.24, 8.76, 13.92, 14.52, and 23.54° primarily, corresponding to crystallographic planes of (010), (011), (01 $\bar{1}$), (012), (202), (022), and (242). Second, Fourier transform infrared (FT-IR) measurement was used to testify functional groups in $L_4Eu^{III}_2Eu^{II}$ for further combining its structure, in which the peaks at 700–1620 and 2915–2954 cm^{-1} corresponded to quinoline aminoaryl²⁹ and tertiary butyl,³⁰ respectively. To be specific, the bands at 2915–2954 cm^{-1} were ascribed to $-CH_3$ (asymmetric stretching vibration), a number of bands at 1615, 1508, 1469, 1386, 1360, 1255, 1160, 1087, 825 and 794 cm^{-1} were ascribed to the quinoline ring, and the strong peak at 1590 cm^{-1} was ascribed to the $C=N$ group; moreover, peaks at 1246 and 3440 cm^{-1} were identified as phenolic $C-O$ and $O-H$ stretching vibrations (Figure 1B).^{29,30} After coordinating with $Eu^{2+/3+}$, the spectrum was red-shifted and the intensity had increased, which explained the success of coordination and the strengthening of the delocalized conjugate system after coordination. To better attest the mixed valence of $L_4Eu^{III}_2Eu^{II}$, a compositional study was performed by using

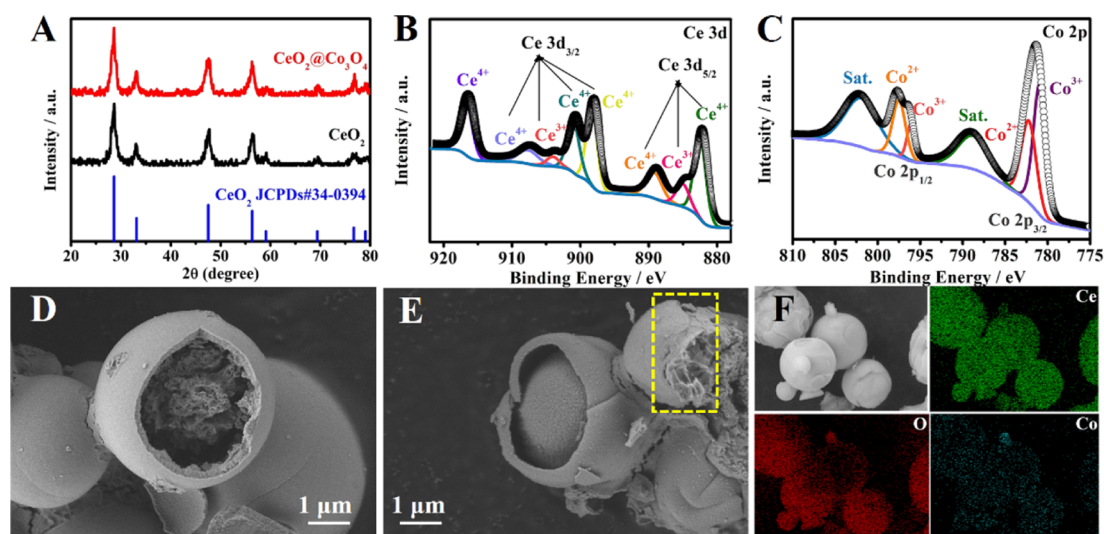


Figure 2. (A) XRD pattern of as-synthesized CeO_2 , $\text{CeO}_2@\text{Co}_3\text{O}_4$, and simulated CeO_2 . XPS spectra in the (B) Ce 3d and (C) Co 2p regions for $\text{CeO}_2@\text{Co}_3\text{O}_4$ TSMs. (D,E) SEM images of CeO_2 and $\text{CeO}_2@\text{Co}_3\text{O}_4$, respectively. (F) SEM images of $\text{CeO}_2@\text{Co}_3\text{O}_4$ and energy-dispersive X-ray elemental mapping images of Ce, O, and Co for $\text{CeO}_2@\text{Co}_3\text{O}_4$.

X-ray photoelectron spectroscopy (XPS). The survey spectrum is shown in Figure S1, and the high-resolution Eu 3d spectrum is shown in Figure 1C. As can be seen from Figure 1C, the two energy levels severally split into two peaks, and the intensity of each front peak was higher than their respective rear peak, indicating the presence of two kinds of chemical state for Eu in $\text{L}_4\text{Eu}^{\text{III}}\text{Eu}^{\text{II}}$,³¹ and the Eu^{3+} matching the peaks at 1133.5 and 1163.0 eV,^{31,32} contained 2.5 times as much as Eu^{2+} matching the peaks at 1123.3 and 1155.0 eV,^{31,32} in which their contents were 71.59 and 28.42%, respectively. These outcomes can be assumed to be due to the ligand redistribution reaction between $\text{Eu}[\text{N}(\text{SiMe}_3)_2]_3$ and complex $\text{L}_3\text{Eu}^{\text{III}}$ and the following partial reduction reaction:²⁸ (i) the silylamine elimination reaction occurred between H_2L and $\text{Eu}[\text{N}(\text{SiMe}_3)_2]_3$ accompanied by the production of binuclear complex $\text{L}_3\text{Eu}^{\text{III}}$; (ii) then, $\text{L}_3\text{Eu}^{\text{III}}$ reacted with $\text{Eu}[\text{N}(\text{SiMe}_3)_2]_3$ to acquire the trinuclear lanthanide amide $(\text{L}_2\text{Eu})_2\text{EuN}(\text{SiMe}_3)_2$ as the intermediate through a ligand redistribution reaction; and (iii) the fracture of Eu–N bonds contributed to the partial reduction of Eu^{3+} to Eu^{2+} , thus forming the mixed-valent trinuclear complex $\text{L}_4\text{Eu}^{\text{III}}_2\text{Eu}^{\text{II}}$, and in theory, the number of Eu^{3+} should be twice that of Eu^{2+} (Scheme 1A).

As far as the UV–vis spectra are concerned (Figure 1D), two distinct absorption peaks at 389 and 511 nm, respectively, were both attributed to $\text{L}_4\text{Eu}^{\text{III}}_2\text{Eu}^{\text{II}}$ absorption (blue curve), and the peak at 572 nm was identified as the characteristic peak of $\text{Fe}_3\text{O}_4@\text{Au}$ (red curve).³³ After compositing with $\text{Fe}_3\text{O}_4@\text{Au}$, the slight red shift of the three characteristic absorption peaks meant the strengthening of the conjugate degree. Even more, the scanning electron microscopy (SEM) images showed that $\text{L}_4\text{Eu}^{\text{III}}_2\text{Eu}^{\text{II}}$ exhibited an irregular block structure composed of sheets with dozens of nanometers stacked tightly together (Figure 1E). As shown in Figure 1F, the synthesized $\text{Fe}_3\text{O}_4@\text{Au}$ nanospheres of about 200 nm in diameter were profusely and tightly loaded on $\text{L}_4\text{Eu}^{\text{III}}_2\text{Eu}^{\text{II}}$. The aforementioned proofs integrally and convincingly demonstrated the successful preparation of $\text{L}_4\text{Eu}^{\text{III}}_2\text{Eu}^{\text{II}}$ and the successful load of $\text{Fe}_3\text{O}_4@\text{Au}$. Finally, the ECL characteristic peak of $\text{L}_4\text{Eu}^{\text{III}}_2\text{Eu}^{\text{II}}-\text{Fe}_3\text{O}_4@\text{Au}$ was located on the short-

wavelength NIR region at about 900 nm (Figure 1D, green curve), which illustrated the successful synthesis of $\text{L}_4\text{Eu}^{\text{III}}_2\text{Eu}^{\text{II}}-\text{Fe}_3\text{O}_4@\text{Au}$ NIFP that also acted as an ECL luminophore.

Characterizations of $\text{CeO}_2@\text{Co}_3\text{O}_4$ TSMs. XRD was utilized to study the crystalline structure of the $\text{CeO}_2@\text{Co}_3\text{O}_4$ TSMs (Figure 2A). All diffraction peaks of the as-prepared CeO_2 can be well matched with fluorite-phase CeO_2 (JCPDS no. 34-0394); in detail, the diffraction peaks at $2\theta = 28.26$, 33.08, 47.48, 56.33, 59.09, 69.40, 76.70, and 79.07° correspond well to the characteristic (111), (200), (220), (311), (222), (400), (331), and (420) crystallographic planes. The XRD pattern of $\text{CeO}_2@\text{Co}_3\text{O}_4$ only showed a slight change after joining with Co_3O_4 , indicating uniform distribution of Co_3O_4 on the CeO_2 surface.²¹ Moreover, the heightening of the peaks manifested the strengthening of crystallinity of the composite. The explicit valence state of the element in the prepared $\text{CeO}_2@\text{Co}_3\text{O}_4$ was tested via XPS measurements. The XPS survey spectrum is shown in Figure S3. In the spectrogram of the Ce element (Figure 2B), the peaks located at 885.0, 882.5, and 889.3 eV belonged to $\text{Ce}^{3+} 3d_{5/2}$ and $\text{Ce}^{4+} 3d_{5/2}$, and the peaks located at 904.1, 898.4, 900.1, and 907.8 eV corresponded to $\text{Ce}^{4+} 3d_{3/2}$ and $\text{Ce}^{3+} 3d_{3/2}$, respectively. As can be seen in Figure 2C, two evident Co 2p_{1/2} peaks appeared at 796.1 and 797.5 eV, along with the high-intensity shake-up satellite peaks (~788.9 and 802.1 eV, denoted as “sat.”) with a band gap of 13.2 eV, all of which are the exclusive traits of Co_3O_4 . Moreover, the fitting peaks at 781.0 and 782.3 eV corresponded to Co^{3+} and Co^{2+} of Co 2p_{3/2}, respectively.^{22,34} These phenomena substantiated the successful preparation of $\text{CeO}_2@\text{Co}_3\text{O}_4$ and contained two redox pairs.

The SEM images in Figure 2D showed that the as-obtained CeO_2 microspheres have a uniform core–shell texture with an average diameter of 4 μm , in which the shell had a thickness of 500 nm. In the broken microsphere, the observed bird-nest-shaped core was composed of dense hairline nanoneedles with about 1 nm thickness. After the introduction of Co_3O_4 species, the morphology of the composite changed into TSMs. In the image marked by the yellow box in Figure 2E, we can see the obvious triple-shelled core–shell structure, and the innermost

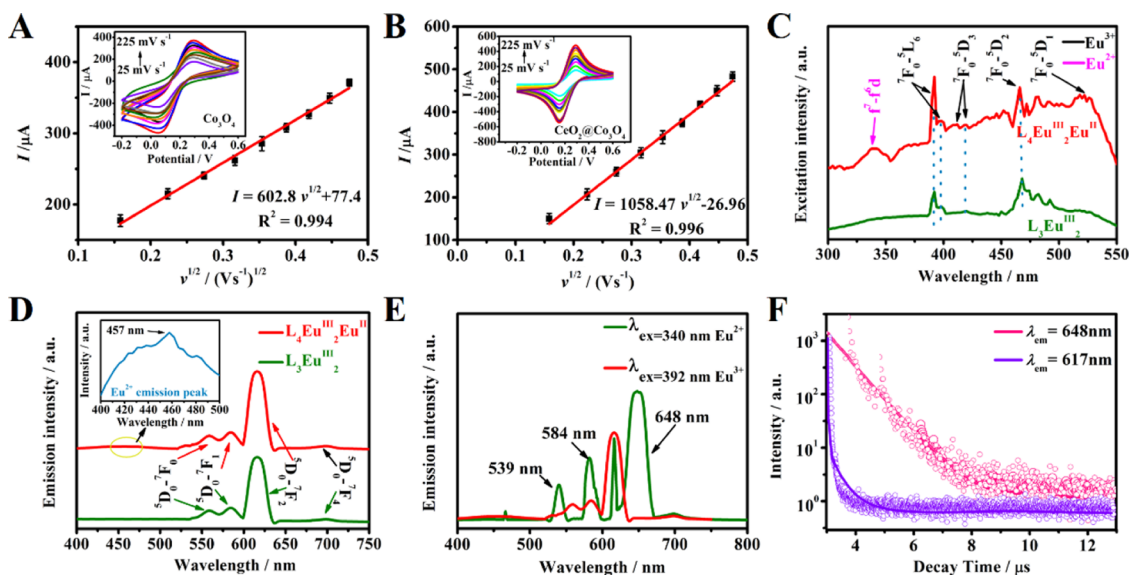


Figure 3. CV curves and linear relations of electrodes modified with (A) Co_3O_4 and (B) $\text{CeO}_2@\text{Co}_3\text{O}_4$ TSMs in 5.0 mmol/L of $[\text{Fe}(\text{CN})_6]^{4-/3-}$ in the scan rate range of 25–225 mV/s. Error bars = SD ($n = 3$). (C) Comparison of excitation spectra of $\text{L}_4\text{Eu}^{\text{III}}_2\text{Eu}^{\text{II}}$ (red) and $\text{L}_3\text{Eu}^{\text{III}}_2$ (green). (D) Comparison of emission spectra of $\text{L}_4\text{Eu}^{\text{III}}_2\text{Eu}^{\text{II}}$ (red) and $\text{L}_3\text{Eu}^{\text{III}}_2$ (green), and the inset figure shows the emission spectra of Eu^{2+} in $\text{L}_4\text{Eu}^{\text{III}}_2\text{Eu}^{\text{II}}$ (under an excitation wavelength of 392 nm). (E) Comparison of emission spectra of $\text{L}_4\text{Eu}^{\text{III}}_2\text{Eu}^{\text{II}}$ under different excitation wavelengths. (F) Lifetime decay curves of Eu^{3+} in $\text{L}_4\text{Eu}^{\text{III}}_2\text{Eu}^{\text{II}}$ under 648 nm (pink, excited by Eu^{2+} at 340 nm) and 617 nm (purple, excited by Eu^{3+} at 392 nm).

layer still presented a bird-nest shape. Furthermore, according to the XRD analysis and the energy-dispersive spectrometry (EDS) images (Figures 2F and S4) of the composite shell, it can be seen that Co_3O_4 and CeO_2 together formed the outermost shell (the EDS of the pure CeO_2 shell only detected the presence of the Ce element). Interestingly, the size of holistic microspheres shrank from 4 to 3.6 μm and the outermost and middle (shell of CeO_2 microspheres) shells were both held at 250 nm approximately. In accord with the result of XRD, Co_3O_4 species were evenly distributed across the shells of $\text{CeO}_2@\text{Co}_3\text{O}_4$, and this result can be easy to obtain from EDS in Figure 2F.

Increased Catalysis of $\text{CeO}_2@\text{Co}_3\text{O}_4$ TSMs. In Figure 2E,F, the overall reduction in size of $\text{CeO}_2@\text{Co}_3\text{O}_4$, the thinning of shell walls, and the increased yolk core together facilitated the increase of catalysis of $\text{CeO}_2@\text{Co}_3\text{O}_4$ TSMs on account of the occurrence of a synergistic effect and the increment of the electroactive surface area and electron-transfer rate. For proving these results, the values of the electroactive surface area of CeO_2 and $\text{CeO}_2@\text{Co}_3\text{O}_4$ were calculated on the basis of cyclic voltammetry (CV) by the Randles–Sevcik equation³⁵

$$I = 2.69 \times 10^5 AD^{1/2} n^3 v^{1/2} c$$

and the cyclic voltammogram was measured under a $\text{K}_3[\text{Fe}(\text{CN})_6]$ environment.

Specifically, I is the peak reduction current of $\text{K}_3[\text{Fe}(\text{CN})_6]$, A is the electrochemical active area (cm^2) to be computed, and D is the diffusion coefficient of $[\text{Fe}(\text{CN})_6]^{4-/3-}$ at 25 $^\circ\text{C}$, which is about $6.70 \times 10^{-6} \text{ cm}^2 \text{ s}^{-1}$. n and v are the values of electron transfer and scanning rate during this test, respectively, and c is the concentration of the $\text{K}_3[\text{Fe}(\text{CN})_6]$ solution.

As shown in Figure 3A,B, the linear fitting equations of CeO_2 and $\text{CeO}_2@\text{Co}_3\text{O}_4$ are $I = 602.8v^{1/2} + 77.4$ and $I = 1058.47v^{1/2} - 26.96$, respectively ($R^2 = 0.994/0.996$). According to slopes, the calculated values of the electro-

chemical active area, respectively, are 17.3 and 30.4 mm^2 , and the oxidation peak current value of $\text{CeO}_2@\text{Co}_3\text{O}_4$ was also superior to that of merely CeO_2 , demonstrating that $\text{CeO}_2@\text{Co}_3\text{O}_4$ possessed the electrochemical active area and electron-transfer rate that are more conducive to catalysis.

Sensitization of Eu^{2+} to Eu^{3+} . In the excitation spectrum of Figure 3C, a strong excitation broadband peak at 340 nm, which was derived from the $4f^7-4f^65d^1$ transition of Eu^{2+} , was observed except the four characteristic excitation peaks belonging to Eu^{3+} . The main peaks at 392, 416, 466, and 522 nm originated from the Eu^{3+} transition of ${}^7\text{F}_0-{}^5\text{L}_6$, ${}^7\text{F}_0-{}^5\text{D}_3$, ${}^7\text{F}_0-{}^5\text{D}_2$, and ${}^7\text{F}_0-{}^5\text{D}_1$, respectively.¹ Interestingly, the excitation broadband peak at 340 nm was not observed in the excitation spectrum of $\text{L}_3\text{Eu}^{\text{III}}_2$, which indicated that Eu^{2+} contributed to the stimulation of $\text{L}_4\text{Eu}^{\text{III}}_2\text{Eu}^{\text{II}}$, yet the stimulation of Eu^{3+} dominated. As can be seen from Figure 3D, compared with the emission of $\text{L}_3\text{Eu}^{\text{III}}_2$, an extremely faint emission broadband of 457 nm that was triggered by the $5d-4f$ transition of Eu^{2+} was captured in the spectrogram of $\text{L}_4\text{Eu}^{\text{III}}_2\text{Eu}^{\text{II}}$ and along with stable Eu^{3+} emission peaks at 559, 584, 616, and 698 nm; meanwhile, the emission peak intensity of $\text{L}_4\text{Eu}^{\text{III}}_2\text{Eu}^{\text{II}}$ was 1.2 times higher than that of unreduced MOF $\text{L}_3\text{Eu}^{\text{III}}_2$. Furthermore, the emission spectrum under Eu^{2+} excitation wavelength (340 nm), distinguishing from that under the maximum emission wavelength of Eu^{3+} (392 nm), possessed three new emission peaks at 539, 584, and 648 nm (Figure 3E). These three new peaks originated from the ${}^5\text{D}_{0,1,2}-{}^7\text{F}_J$ transition of Eu^{3+} , and no Eu^{2+} emission peak was observed. These meant that Eu^{2+} in the synthesized $\text{L}_4\text{Eu}^{\text{III}}_2\text{Eu}^{\text{II}}$ can sensitize Eu^{3+} and increase the luminescence intensity of $\text{L}_4\text{Eu}^{\text{III}}_2\text{Eu}^{\text{II}}$.^{1,36,37} The PL quantum yield of $\text{L}_4\text{Eu}^{\text{III}}_2\text{Eu}^{\text{II}}$ was 10%, and this sensitization efficiency is higher than those reported in some literature studies.^{11,38}

To attest the stimuli response in spatial–temporal dimensions of $\text{L}_4\text{Eu}^{\text{III}}_2\text{Eu}^{\text{II}}$, the luminescence decay curves of emissions of Eu^{3+} at 648 nm (excited by Eu^{2+} at 340 nm) and 617 nm (excited by Eu^{3+} at 392 nm) were tested. In Figure 3F,

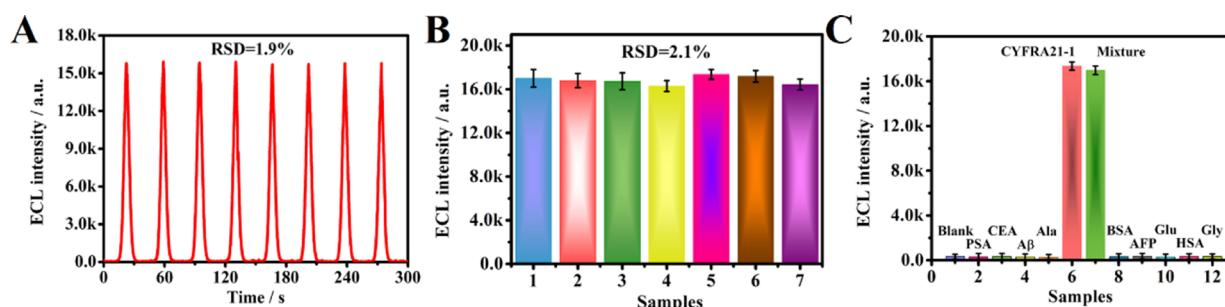


Figure 5. (A) Operation stability of the prepared biosensor under continuous potential scanning (eight scans). (B) Repeatability of the biosensor under the detection of seven different electrodes. (C) Selectivity tests of biosensors for different interferences (10 ng/mL). Error bars = SD ($n = 3$).

observed in the corresponding ECL intensity–time curve (Figure 4A). In addition, more digitized, visualized, and exact demonstration was shown via linear equation (logarithm of CYFRA 21-1 concentration and ECL intensity were for abscissa and ordinate, respectively), which was expressed by $I = 1442.38 \lg c + 5702.16$, whose correlation coefficient was 0.996 (Figure 4B). The proposed NIR ECL biosensor owned a broad examination area from 5 fg/mL to 100 ng/mL with a low LOD of 1.70 fg/mL. Compared with other detection methods, the ultrasensitive superiority of the NIR ECL detection method was embodied (Table S1), endowing the NIR ECL biosensor with an excellent prospect in bioimmunoassay. The detection limit is lower than most of the previously reported ECL biosensors, which means that the ECL biosensor has a high sensitivity in the detection of CYFRA 21-1. Simultaneously, the biosensor owns a wide detection range, and the normal critical value (<3.3 ng/mL) of CYFRA 21-1 is much higher than the detection limit and is in the detection range, which makes the biosensor meet the requirement for the diagnosis of disease completely.

Speculation of the ECL-Enhanced Mechanism. The sensitization of Eu^{2+} to Eu^{3+} endowed the luminophore led by NIR $\text{L}_4\text{Eu}^{\text{III}}_2\text{Eu}^{\text{II}}$ with a stronger luminescent intensity than single Eu^{3+} or H_2L or even $\text{L}_3\text{Eu}^{\text{III}}_2$. This conclusion can be drawn from the comparison of ECL–potential curves in Figure 4C, in which the ECL intensities of $\text{L}_4\text{Eu}^{\text{III}}_2\text{Eu}^{\text{II}}$, $\text{L}_3\text{Eu}^{\text{III}}_2$, Eu^{3+} , and H_2L were 11,530.4, 7423.40, 1072.75, and 1055.25 a.u., respectively. The increasing luminous efficiency of $\text{L}_3\text{Eu}^{\text{III}}_2$ is surpassed trebly and much for Eu^{3+} and H_2L , which resulted from the antenna effect that was generated by the energy transfer from a high conjugated structure H_2L to Eu^{3+} and also occurred in $\text{L}_4\text{Eu}^{\text{III}}_2\text{Eu}^{\text{II}}$. From Figure 4D, it can be observed that the ECL–potential curves conformed to the comparative result of calculative electrochemical active areas; that is, distinct comparison of bare $\text{L}_4\text{Eu}^{\text{III}}_2\text{Eu}^{\text{II}}$, $\text{L}_4\text{Eu}^{\text{III}}_2\text{Eu}^{\text{II}}-\text{Co}_3\text{O}_4$ system, $\text{L}_4\text{Eu}^{\text{III}}_2\text{Eu}^{\text{II}}-\text{CeO}_2$ system, and $\text{L}_4\text{Eu}^{\text{III}}_2\text{Eu}^{\text{II}}-\text{CeO}_2@ \text{Co}_3\text{O}_4$ system with ECL intensities of 11,530.40, 12,683.44, 14,030.40, and 17,349.15 a.u., respectively, was displayed. Motivated by the high catalytic performance resulted from strong synergistic effects and interfacial effects in $\text{CeO}_2@ \text{Co}_3\text{O}_4$ TSMs, the dual catalytic effects of $\text{Ce}^{3+}/\text{Ce}^{4+}$ and $\text{Co}^{2+}/\text{Co}^{3+}$ on $\text{S}_2\text{O}_8^{2-}$ were further strengthened. The reaction of Co^{2+} and $\text{S}_2\text{O}_8^{2-}$ generated $\text{SO}_4^{\bullet-}$ at the same time as Co^{3+} , and then, Co^{3+} further reacted to generate OH^\bullet and was converted back to Co^{2+} , and the generated OH^\bullet reacted with $\text{S}_2\text{O}_8^{2-}$ to produce more $\text{SO}_4^{\bullet-}$ for a stronger ECL intensity. The reaction mechanism of $\text{Ce}^{3+}/\text{Ce}^{4+}$ is similar to that of $\text{Co}^{2+}/\text{Co}^{3+}$ but lacked the independent catalysis of Co^{2+} to

$\text{S}_2\text{O}_8^{2-}$. The whole conjectural ECL mechanism^{42–44} is shown as follows in the form of equations and Scheme 1D

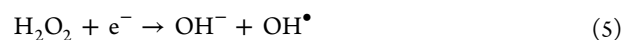
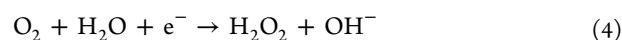
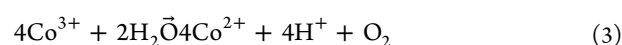
Path 1



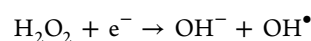
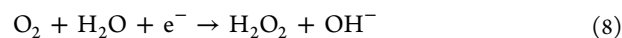
Path 2



Path 3



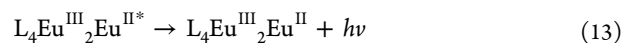
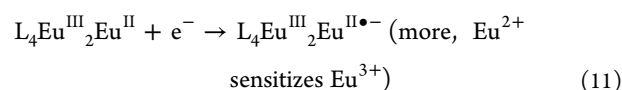
Simultaneous path 3



or



ECL emission



On one hand, we compared ECL signals of bare $\text{L}_4\text{Eu}^{\text{III}}_2\text{Eu}^{\text{II}}$ system and $\text{L}_4\text{Eu}^{\text{III}}_2\text{Eu}^{\text{II}}-\text{CeO}_2@ \text{Co}_3\text{O}_4$ system in $\text{K}_2\text{S}_2\text{O}_8$ and PBS coreactant, trying to figure out the catalytic object of $\text{CeO}_2@ \text{Co}_3\text{O}_4$. As can be seen in Figure 4C,D, the ECL intensities of the bare $\text{L}_4\text{Eu}^{\text{III}}_2\text{Eu}^{\text{II}}$ system and $\text{L}_4\text{Eu}^{\text{III}}_2\text{Eu}^{\text{II}}-\text{CeO}_2@ \text{Co}_3\text{O}_4$ system in $\text{K}_2\text{S}_2\text{O}_8$ were 11,530.40 and 17,349.15 a.u., respectively, but low and indiscriminate values with 879.375 and 1072.75 a.u. were observed when the coreactant was PBS, indicating the sole catalysis of $\text{CeO}_2@ \text{Co}_3\text{O}_4$ for $\text{K}_2\text{S}_2\text{O}_8$ rather than acting on $\text{L}_4\text{Eu}^{\text{III}}_2\text{Eu}^{\text{II}}$.

Demonstration of the As-Fabricated Biosensor for Stability, Repeatability, and Selectivity. Stability, repeatability, and selectivity, three crucial indexes in the evaluation process for a biosensor, were utilized as a judgment standard for the practicability of the biosensor. The stability test was carried out by eight continuous cycles of electrode scanning, the reproducibility test was carried out via the ECL performance test of seven different electrodes loaded with the same amount of materials, and at last, the selectivity test was conducted for different interferences and mixtures that contained targeted CYFRA 21-1 and whole interferences (Figure 5A–C). As can be seen from Figure 5A,B, whether the test was performed under multiple cycles on the same electrode or conducted via different electrodes in the same environment, both the measured ECL intensities had tiny differences with outstanding relative standard deviations (RSDs) of 2.1 and 1.9%, respectively. These demonstrated that the proposed ECL biosensor possesses preeminent stability and reproducibility. For selectivity, the measured ECL intensities between other interferences and CYFRA 21-1 had a tremendous difference, in which the values when tested resulted in very low interferences unlike that when testing the value of CYFRA 21-1 (17,349.15 a.u.). Moreover, the detection signal with the mixture (1 ng/mL of CYFRA 21-1 + 10 ng/mL of interferences) was almost the same as the detection signal with CYFRA 21-1, which confirmed the terrific selectivity of the ECL biosensor (Figure 5C). These three excellent properties provided a great possibility in practical application for the proposed NIR ECL biosensor.

Analysis of Real Samples. To demonstrate the practical application of the biosensor, three real serum samples from local hospitals, human serum samples, were utilized as initial samples to conduct the standard recovery test. Prior to the measurement, the samples were centrifuged to obtain the supernatant (9000 rpm, two times). The concentrations of CYFRA 21-1 in the obtained human serum were 1.440, 5.130, and 8.560 ng/mL, and after testing, the calculated recovery rates were located in the range of 98.40–100.8% with a low RSD from 0.73 to 2.7% (Table S2). Meanwhile, enzyme-linked immunosorbent assay (ELISA) was used as a reference method to validate the proposed method. In comparison with the ELISA kit, the detection results of the as-fabricated biosensor showed no obvious difference. There would be a promising future for the proposed biosensor in clinical detection of CYFRA 21-1.

CONCLUSIONS

The novel NIR ECL biosensor that was based on the sensitization of Eu^{2+} to Eu^{3+} was successfully constructed for the ultrasensitive detection of CYFRA 21-1, in which $\text{L}_4\text{Eu}^{\text{III}}_2\text{Eu}^{\text{II}}$ with the characteristic fluorescence in the NIR region was used as a luminophore and $\text{CeO}_2@\text{Co}_3\text{O}_4$ TSMs were used as the catalyst. The employed amine elimination reaction strategy with a peculiar two-coordination environment ligand H_2L avoided a drawback that Eu^{2+} is easily oxidized into Eu^{3+} and made $\text{L}_4\text{Eu}^{\text{III}}_2\text{Eu}^{\text{II}}$ enhance the luminescent intensity by the sensitization of Eu^{2+} to Eu^{3+} , thereby realizing self-enhanced luminescence. In addition, the characteristic fluorescence of $\text{L}_4\text{Eu}^{\text{III}}_2\text{Eu}^{\text{II}}$ fell in the NIR region of 900 nm, so $\text{L}_4\text{Eu}^{\text{III}}_2\text{Eu}^{\text{II}}$ was used as a NIFP to participate in the construction of the ECL biosensor to reduce the damage to the test sample and improve the sensitivity of the biosensor. Moreover, the TSMs structure of $\text{CeO}_2@\text{Co}_3\text{O}_4$ owned a very

outstanding catalytic performance to promote the generation of more $\text{SO}_4^{\bullet-}$ radicals, such that the ECL strength was further improved. This NIR ECL biosensor possessed a low LOD of 1.70 fg/mL, and the novel mixed-valence Eu-MOF luminophore added a new member for the self-enhanced luminescence family. The constructed biosensor that combined with a NIFP provided feasible tactics to achieve efficient and sensitive ECL immunodetection.

ASSOCIATED CONTENT

Supporting Information

The Supporting Information is available free of charge at <https://pubs.acs.org/doi/10.1021/acs.analchem.1c01531>.

Chemicals and apparatus; synthesis of $\text{Fe}_3\text{O}_4@\text{AuNPs}$; electrodeposition of Au on the electrode; XPS survey spectrum of as-prepared $\text{L}_4\text{Eu}^{\text{III}}_2\text{Eu}^{\text{II}}$ and $\text{CeO}_2@\text{Co}_3\text{O}_4$ TSMs; SEM elemental mapping of C, Eu, O, and N for $\text{L}_4\text{Eu}^{\text{III}}_2\text{Eu}^{\text{II}}$ and Ce and O for CeO_2 ; optimization of experimental conditions; CV and EIS characterization of stepwise biosensor fabrication; stability tests of biosensors for different concentrations of CYFRA 21-1; comparison of sensitivity of different methods and analysis of real samples; standard addition and ELISA data of the proposed biosensor for CYFRA 21-1 detection; and comparison of the ECL yield of different luminophores in $\text{K}_2\text{S}_2\text{O}_8$ (PDF)

AUTHOR INFORMATION

Corresponding Author

Dan Wu – Collaborative Innovation Centre for Green Chemical Manufacturing and Accurate Detection School of Chemistry and Chemical Engineering, Key Laboratory of Interfacial Reaction & Sensing Analysis in Universities of Shandong, School of Chemistry and Chemical Engineering, University of Jinan, Jinan 250022, Shandong, China;
orcid.org/0000-0002-8732-5988;
Email: wudan791108@163.com

Authors

Lu Zhao – Collaborative Innovation Centre for Green Chemical Manufacturing and Accurate Detection School of Chemistry and Chemical Engineering, Key Laboratory of Interfacial Reaction & Sensing Analysis in Universities of Shandong, School of Chemistry and Chemical Engineering, University of Jinan, Jinan 250022, Shandong, China

Xianzhen Song – Collaborative Innovation Centre for Green Chemical Manufacturing and Accurate Detection School of Chemistry and Chemical Engineering, Key Laboratory of Interfacial Reaction & Sensing Analysis in Universities of Shandong, School of Chemistry and Chemical Engineering, University of Jinan, Jinan 250022, Shandong, China

Xiang Ren – Collaborative Innovation Centre for Green Chemical Manufacturing and Accurate Detection School of Chemistry and Chemical Engineering, Key Laboratory of Interfacial Reaction & Sensing Analysis in Universities of Shandong, School of Chemistry and Chemical Engineering, University of Jinan, Jinan 250022, Shandong, China;
orcid.org/0000-0002-4321-4282

Dawei Fan – Collaborative Innovation Centre for Green Chemical Manufacturing and Accurate Detection School of Chemistry and Chemical Engineering, Key Laboratory of Interfacial Reaction & Sensing Analysis in Universities of

Shandong, School of Chemistry and Chemical Engineering, University of Jinan, Jinan 250022, Shandong, China

Qin Wei – Collaborative Innovation Centre for Green Chemical Manufacturing and Accurate Detection School of Chemistry and Chemical Engineering, Key Laboratory of Interfacial Reaction & Sensing Analysis in Universities of Shandong, School of Chemistry and Chemical Engineering, University of Jinan, Jinan 250022, Shandong, China;

orcid.org/0000-0002-3034-8046

Complete contact information is available at:

<https://pubs.acs.org/10.1021/acs.analchem.1c01531>

Notes

The authors declare no competing financial interest.

ACKNOWLEDGMENTS

This work was supported by the Young Taishan Scholars Program of Shandong Province (tsqn201909124), the National Natural Science Foundation of China (21775054), the Project of “20 items of University” of Jinan (2019GXRC018), and the National Key Scientific Instrument and Equipment Development Project of China (21627809). All of the authors express their sincere thanks.

REFERENCES

- (1) Bansal, A. K.; Antolini, F.; Zhang, S.; Stroea, L.; Ortolani, L.; Lanzi, M.; Serra, E.; Allard, S.; Scherf, U.; Samuel, I. D. W. *J. Phys. Chem. C* **2016**, *120*, 1871–1880.
- (2) Liu, J.; Sun, Y.-Q.; Wang, P.; Zhang, J.; Guo, W. *Analyst* **2013**, *138*, 2654–2660.
- (3) Huang, J.; Pu, K. *Angew. Chem., Int. Ed.* **2020**, *59*, 11717–11731.
- (4) Zheng, J.; Xu, Y.; Fan, L.; Qin, S.; Li, H.; Sang, M.; Li, R.; Chen, H.; Yuan, Z.; Li, B. *Small* **2020**, *16*, 2002211.
- (5) Huang, J.; Jiang, Y.; Li, J.; Huang, J.; Pu, K. *Angew. Chem., Int. Ed.* **2021**, *60*, 3999–4003.
- (6) Song, X.; Li, X.; Wei, D.; Feng, R.; Yan, T.; Wang, Y.; Ren, X.; Du, B.; Ma, H.; Wei, Q. *Biosens. Bioelectron.* **2019**, *126*, 222–229.
- (7) Hu, L.; Xu, G. *Chem. Soc. Rev.* **2010**, *39*, 3275–3304.
- (8) Fu, L.; Fu, K.; Gao, X.; Dong, S.; Zhang, B.; Fu, S.; Hsu, H.-Y.; Zou, G. *Anal. Chem.* **2021**, *93*, 2160–2165.
- (9) Bünzli, J.-C. G.; Piguët, C. *Chem. Soc. Rev.* **2005**, *34*, 1048–1077.
- (10) Xu, S.; Wang, Z.; Li, P.; Li, T.; Bai, Q.; Sun, J.; Yang, Z. *J. Am. Ceram. Soc.* **2017**, *100*, 2069–2080.
- (11) Vela, J.; Prall, B. S.; Rastogi, P.; Werder, D. J.; Casson, J. L.; Williams, D. J.; Klimov, V. I.; Hollingsworth, J. A. *J. Phys. Chem. C* **2008**, *112*, 20246–20250.
- (12) Zhang, X.; Zhu, Q.; Chen, B.; Wang, S. X.; Rogach, A. L.; Wang, F. *Adv. Photonics Res.* **2021**, *2*, 2000089.
- (13) Zhao, L.; Kuang, X.; Chen, C.; Sun, X.; Wang, Z.; Wei, Q. *Chem. Commun.* **2019**, *55*, 10170–10173.
- (14) Tang, Q.; Qiu, K.; Li, J.; Zhang, W.; Zeng, Y. *J. Mater. Sci.: Mater. Electron.* **2017**, *28*, 18686–18696.
- (15) Garfield, D. J.; Borys, N. J.; Hamed, S. M.; Torquato, N. A.; Tajon, C. A.; Tian, B.; Shevitski, B.; Barnard, E. S.; Suh, Y. D.; Aloni, S.; Neaton, J. B.; Chan, E. M.; Cohen, B. E.; Schuck, P. J. *Nat. Photonics* **2018**, *12*, 402–407.
- (16) Huang, P.; Chen, D.; Wang, Y. *J. Alloys Compd.* **2011**, *509*, 3375–3381.
- (17) Saradhi, M. P.; Boudin, S.; Varadaraju, U. V.; Raveau, B. *J. Solid State Chem.* **2010**, *183*, 2496–2500.
- (18) Jiao, M.; Xu, Q.; Liu, M.; Yang, C.; Yu, Y. *Phys. Chem. Chem. Phys.* **2018**, *20*, 26995–27002.
- (19) Le, H.-J.; Van Dao, D.; Yu, Y.-T. *J. Mater. Chem. A* **2020**, *8*, 12968–12974.
- (20) Dao, D. V.; Adilbish, G.; Le, T. D.; Nguyen, T. T. D.; Lee, I.-H.; Yu, Y.-T. *J. Catal.* **2019**, *377*, 589–599.

(21) Zhang, L.; Zhang, L.; Xu, G.; Zhang, C.; Li, X.; Sun, Z.; Jia, D. *New J. Chem.* **2017**, *41*, 13418–13424.

(22) Wang, X.; Liu, M.; Yu, H.; Zhang, H.; Yan, S.; Zhang, C.; Liu, S. *J. Mater. Chem. A* **2020**, *8*, 22886–22892.

(23) Zhao, H.; Dong, Y.; Jiang, P.; Wang, G.; Zhang, J. *ACS Appl. Mater. Interfaces* **2015**, *7*, 6451–6461.

(24) Huang, F.; Wang, J.; Chen, W.; Wan, Y.; Wang, X.; Cai, N.; Liu, J.; Yu, F. *J. Taiwan Inst. Chem. Eng.* **2018**, *83*, 40–49.

(25) Zou, W.; Ge, C.; Lu, M.; Wu, S.; Wang, Y.; Sun, J.; Pu, Y.; Tang, C.; Gao, F.; Dong, L. *RSC Adv.* **2015**, *5*, 98335–98343.

(26) Wang, Y.; Zhao, G.; Chi, H.; Yang, S.; Niu, Q.; Wu, D.; Cao, W.; Li, T.; Ma, H.; Wei, Q. *J. Am. Chem. Soc.* **2021**, *143*, 504–512.

(27) Lu, N.; Gao, A.; Dai, P.; Mao, H.; Zuo, X.; Fan, C.; Wang, Y.; Li, T. *Anal. Chem.* **2015**, *87*, 11203–11208.

(28) Jiang, Y.; Zhu, X.; Chen, M.; Wang, Y.; Yao, Y.; Wu, B.; Shen, Q. *Organometallics* **2014**, *33*, 1972–1976.

(29) Dines, T. J.; Macgregor, L. D.; Rochester, C. H. *Langmuir* **2002**, *77*, 239.

(30) Raj, M.; Padhi, S. K. *J. Heterocycl. Chem.* **2019**, *56*, 988–997.

(31) Hasegawa, T.; Iwaki, M.; Tanaka, R.; Kim, S.-W.; Yin, S.; Toda, K. *Inorg. Chem. Front.* **2020**, *7*, 4040–4051.

(32) Yi, S.; Han, D.; Yuan, Q.; Yang, Q.; Yang, Y.; Zhou, D.-Y.; Feng, L. *J. Mater. Chem. C* **2020**, *8*, 13754–13761.

(33) Cai, H.; Li, K.; Shen, M.; Wen, S.; Luo, Y.; Peng, C.; Zhang, G.; Shi, X. *J. Mater. Chem.* **2012**, *22*, 15110–15120.

(34) Zhang, X.; Lu, Y.; Chen, Q.; Huang, Y. *J. Mater. Chem. B* **2020**, *8*, 6459–6468.

(35) Yang, L.; Jia, Y.; Wu, D.; Zhang, Y.; Ju, H.; Du, Y.; Ma, H.; Wei, Q. *Anal. Chem.* **2019**, *91*, 14066–14073.

(36) Pellé, F.; Gardant, N.; Genotelle, M.; Goldner, P.; Porcher, P. *J. Phys. Chem. Solids* **1995**, *56*, 1003–1012.

(37) Tsai, Y.-Y.; Shih, H.-R.; Tsai, M.-T.; Chang, Y.-S. *Mater. Chem. Phys.* **2014**, *143*, 611–615.

(38) Chengelis, D. A.; Yingling, A. M.; Badger, P. D.; Shade, C. M.; Petoud, S. *J. Am. Chem. Soc.* **2005**, *127*, 16752–16753.

(39) Feng, P.-F.; Kong, M.-Y.; Yang, Y.-W.; Su, P.-R.; Shan, C.-F.; Yang, X.-X.; Cao, J.; Liu, W.-S.; Feng, W.; Tang, Y. *ACS Appl. Mater. Interfaces* **2019**, *11*, 1247–1253.

(40) Liu, X.; Xie, W.; Lü, Y.; Feng, J.; Tang, X.; Lin, J.; Dai, Y.; Xie, Y.; Yan, L. *Inorg. Chem.* **2017**, *56*, 13829–13841.

(41) Chen, F.; Wang, Y.-M.; Guo, W.; Yin, X.-B. *Chem. Sci.* **2019**, *10*, 1644–1650.

(42) Trogadas, P.; Parrondo, J.; Ramani, V. *ACS Appl. Mater. Interfaces* **2012**, *4*, 5098–5102.

(43) Lima, M. M. M.; do Rosário Guimarães, I.; Silveira Vieira, S.; Batista Chagas, P. M.; de Abreu Piva, N. M.; Resende Luiz, M. E.; Terra, J. C.; Tirelli, A. A.; Domingos Ardisson, J. *J. Environ. Chem. Eng.* **2020**, *8*, 103731.

(44) Song, X.; Shao, X.; Dai, L.; Fan, D.; Ren, X.; Sun, X.; Luo, C.; Wei, Q. *ACS Appl. Mater. Interfaces* **2020**, *12*, 9098–9106.